Correlation of the Microstructure and Fracture Toughness of the Heat-Affected Zones of an SA 508 Steel

SANGHO KIM, SUK YOUNG KANG, SEI J. OH, SOON-JU KWON, SUNGHAK LEE, JOO HAG KIM, and JUN HWA HONG

In this study, microstructures of a heat-affected zone (HAZ) of an SA 508 steel were identified by Mossbauer spectroscopy in conjunction with microscopic observations, and were correlated with fracture toughness. Specimens with the peak temperature raised to 1350 °C showed mostly martensite. With the peak temperature raised to 900 °C, the martensite fraction was reduced, while bainite or martensite islands were formed because of the slow cooling from the lower austenite region and the increase in the prior austenite grain size. As the martensite fraction present inside the HAZ increased, hardness and strength tended to increase, whereas fracture toughness decreased. The microstructures were not changed much from the base metal because of the minor tempering effect when it was raised to 650 °C or 700 °C. However, fracture toughness of the subcritical HAZ with the peak temperature raised to 650 °C to 700 °C was seriously reduced after postweld heat treatment (PWHT) because carbide particles were of primary importance in initiating voids. Thus, the most important microstructural factors affecting fracture toughness were the martensite fraction before PWHT and the carbide fraction after PWHT.

I. INTRODUCTION

IN heat-affected zones (HAZ) of an ASME SA 508 steel, a low-alloy steel used for structural components of atomic power plants, microstructural changes such as grain coarsening, carbide precipitation, and martensite formation generally occur and cause a deterioration in toughness and an increase in sensitivity to brittle fracture.[1] Microstructures of the HAZ after large-heat-input welding are affected by factors such as chemical composition, welding condition, and peak reheating temperature. According to the distance from a fusion zone, the HAZ subjected to welding thermal cycles is composed of a coarse-grained region reheated above 1100 °C, a fine-grained region reheated between 900 °C and 1100 °C, a partially transformed region reheated between 700 °C and 900 °C, and a tempered region reheated below 700 °C. Among these HAZ regions, the most vulnerable to embrittlement is the coarse-grained region located near the bond, which is generally referred to as a local brittle zone (LBZ).[2–6] However, in multipass welding, this LBZ can be changed because of a repeated heat effect. Particularly, the multipass welded HAZ shows a very complex microstructure resulting from complicated thermal history, which makes the evaluation of fracture toughness on specific HAZ regions very difficult, and thus thermal-cycle-simulation testing is typically used. In this case, quantitative analyses are also difficult because of the microstructural complexity.[7] The degree of embrittlement in the LBZ varies with material chemistry and welding conditions. Under the conditions for the easy LBZ formation, the LBZ fatally affects toughness of the welded region. Therefore, assuring fracture toughness in this region and quantitatively evaluating it are very critical to the safety of structures. This is particularly so when SA 508 steels are applied to structures for atomic power plants. Many studies have been made on microstructural factors associated with the embrittlement phenomenon,[8–11] but very few can sufficiently explain its mechanism.

Since the HAZ microstructure changes with thermal cycles in a highly complicated manner, quantitative and systematic analyses are extremely difficult.[7] Optical microscopy, electron microscopy, and X-ray diffraction have been used for the microstructural analysis of the HAZ, but its quantitative analysis is hardly possible because of the mixed phases of martensite, bainite, ferrite, austenite, and carbides. Recently, researches using Mossbauer spectroscopy have been actively pursued. The Mossbauer effect refers to the radiation and absorption phenomena of recoilless gamma rays of atomic nucleus, and Mossbauer spectroscopy is conducted by transforming the energy of gamma rays using the Doppler effect.[12,13] This Mossbauer spectroscopy has advantages for performing qualitative and quantitative phase analyses of steels, which are hard to achieve in other analysis techniques mentioned previously.[14–19]

In this study, phases present in the welded HAZ of an SA 508 steel were identified, and their volume fractions were quantitatively measured using Mossbauer spectroscopy. Applicability of Mossbauer spectroscopy to qualitative and quantitative phase analyses of the HAZ was then investigated by comparing microstructural observations with the data obtained from Mossbauer spectroscopy. In addition, mechanisms associated with the embrittlement phenomenon in the HAZ were identified by measuring the absorbed impact energy and by correlating related microstructural factors. These detailed microstructural analyses and toughness evaluation not only contribute to clarifying the embrittlement

SANGHO KIM and SUK YOUNG KANG, Research Assistants, and SUNGHAK LEE, Professor, are with the Center for Advanced Aerospace Materials, Pohang University of Science and Technology, Pohang, 790-784 Korea. SEI J. OH, Postdoctoral Research Associate, and SOON-JU KWON, Professor, are with the Department of Materials Science, Pohang University of Science and Technology, Pohang, 790-784 Korea. JOO HAG KIM, Senior Researcher, and JUN HWA HONG, Director, are with the Nuclear Materials Technology Development Team, Korea Atomic Energy Research Institute, Dajeon, 305-600 Korea.

Manuscript submitted December 14, 1998.

Table I. Chemical Composition of the SA 508 Steel (Class 3) Used (Weight Percent)

C	Si	Mn	P	S	Ni	Cr	Mo	V	Cu	Al	Fe
0.18	0.10	1.46	0.006	0.003	0.86	0.15	0.51	0.004	0.030	0.018	bal

Table II. Room-Temperature Tensile Properties of the SA 508 Steel Used

Yield Strength (MPa)	Tensile Strength (MPa)	Elongation (Pct)	Reduction in Area (Pct)
431	560	29	71

of the HAZ, but also help establish basic alloy-designing conditions required for the development of SA 508 steels and their property improvement.

II. EXPERIMENTAL

An ASME SA 508 steel (class 3) was used in the present study, and its chemical composition is provided in Table I. This base metal was austenitized at 880 °C for 1.5 hours, air cooled (cooling rate: 20 °C/min), and tempered at 660 °C for 10 hours. Its mechanical properties are shown in Table II.

Conventional welding conditions of this steel are listed in Table III, and the calculated heat input is 30 kJ/cm. Welding thermal cycles under these welding conditions were obtained from the thermal-flow formula of Rosenthal,[20] and the results are shown in Figure 1. Based on these thermal cycles, subzone HAZs were classified by segmenting the HAZ into isothermal curves of representative peak temperature, T_p, as shown in Figures 2(a) through (e).[21] These show a unit HAZ model for various welding conditions. This HAZ model depends on HAZ width (W_H) and interlayer space (W_I), which is characterized by material constants and welding conditions, and the W_H/W_I ratio plays an important role in determining the size of a coarse-grained HAZ. Here, *a* through *e* refer to the peak temperature regions divided into 1300 °C $< a <$ melting point, 1100 °C $< b <$ 1300 °C, 900 °C $< c <$ 1100 °C, 700 °C $< d <$ 900 °C, and 600 °C $< e <$ 700 °C, respectively, where *a* and *b* can be classified into coarse-grained HAZ, *c* fine-grained HAZ, *d* intercritical HAZ, and *e* subcritical HAZ. In single-pass welding, the coarse-grained HAZ is clearly visible (Figure 2(a)). Figures 2(b) through (e) indicate the case of multi-pass welding, and are plotted in terms of the W_H/W_I ratio. The microstructure of the N^{th} pass is changed by thermal cycles of previous ($(N-1)^{th}$ or $(N-2)^{th}$) and subsequent ($(N+1)^{th}$ or $(N+2)^{th}$) passes. Since the W_H/W_I ratio of the actual HAZ was measured to be about 0.92, it corresponds to Figure 2(c), which was used to establish HAZ simulation conditions.

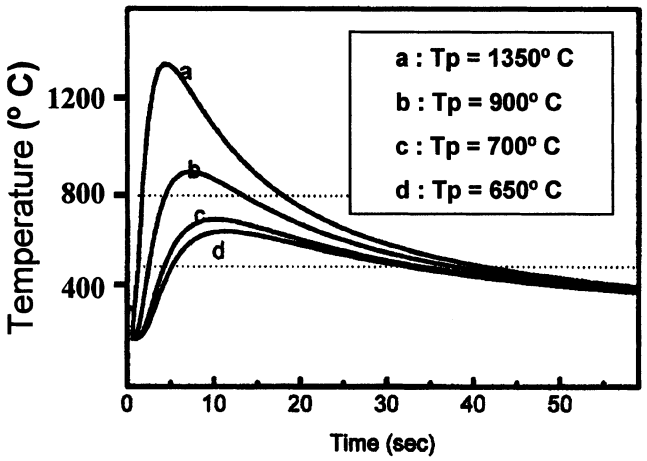

Fig. 1—Thermal cycles for various peak temperatures.

To simulate the HAZ, thermal-cycle-simulation conditions were established as shown in Table IV, based on theoretically calculated thermal cycle, peak temperature, and cooling time between 800 °C and 500 °C ($\Delta t_{8/5}$). A metal thermal-cycle simulator (MTCS), which can control heating and cooling rates, was used for the thermal simulation test. Specimens subjected to double thermal cycles are referred to as A1 through A7 in a decreasing order of T_p, and those subjected to postweld heat treatment (PWHT) at 620 °C for 4.5 hours after the double thermal cycles are referred to as B1 through B7. On these thermally simulated specimens, tensile and Charpy impact tests were conducted. Specimens for these tests were prepared perpendicular to the rolling direction (transverse), and the overall gage section or the notched section was included in the thermally simulated regions. Tensile bars having a gage diameter of 6.35 mm and a gage length of 20 mm were tested at room temperature at a strain rate of 10^{-3}/s using a 10-ton Instron machine. Charpy impact tests were conducted at −50 °C, and absorbed impact energy was measured. The testing temperature of −50 °C was chosen because it is known that the ductile-brittle transition temperature in the actual components for atomic power plants, used at room temperature, increases by about 100 °C due to the irradiation of radioactive rays.[22] Hardness of the simulated HAZ was measured using a Vickers hardness tester under a load of 1 kg.

The simulated HAZ specimens were sectioned, polished, and etched by a nital solution. Their microstructures were

Table III. Welding Conditions of the SA 508 Steel

Process	Wire Diameter (mm)	Current (A)	Voltage (V)	Travel Speed (cm/min)	Preheat Temperature (°C)	Interpass Temperature (°C)	Postweld Heat Treatment
SAW*	4	500 to 600	28 to 32	30 to 40	121	200	615 °C, 40 h

* Submerged arc welding.

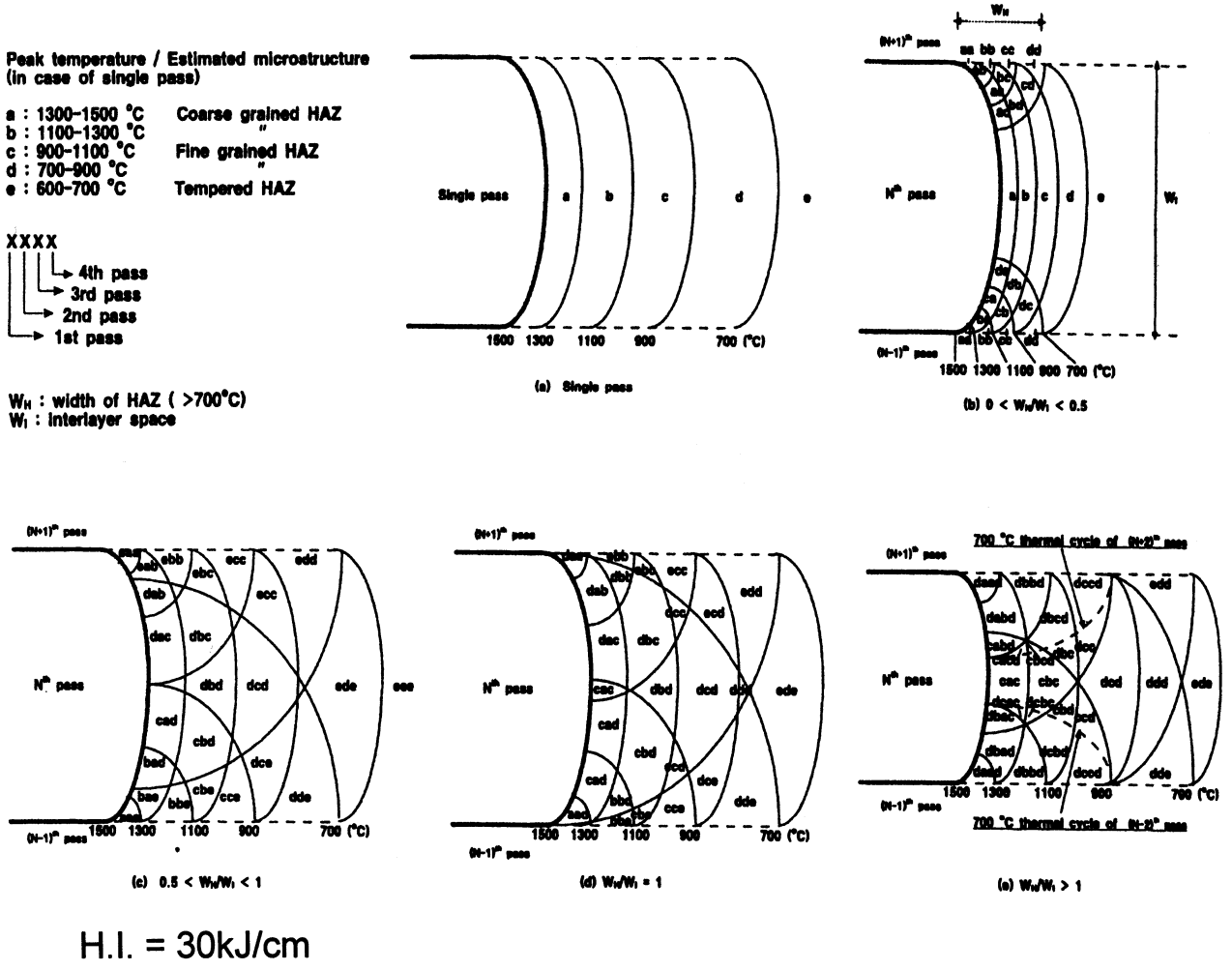

Fig. 2—(*a*) through (*e*) Schematic diagrams showing HAZ isothermals in multipass welding.

Table IV. Thermal Cycle Simulation Conditions for Various HAZ Subzones

Subzone* (Simulated Specimen)	N^{th} Pass Heating Rate (°C/s)	N^{th} Pass Holding Temperature and Time (°C/s, s)	N^{th} Pass Cooling Rate and $\Delta t_{8/5}$** (°C/s, s)	Interpass Temperature (°C)	$(N+1)^{th}$ Pass Heating Rate (°C/s)	$(N+1)^{th}$ Pass Holding Temperature and Time (°C/s, s)	$(N+1)^{th}$ Pass Cooling Rate and $\Delta t_{8/5}$** (°C/s, s)
UCGHAZ (A1)	256	1350, 10	13, 23	200	256	1350, 10	13, 23
SCRCGHAZ (A2)	256	1350, 10	13, 23		256	900, 10	13, 23
ICRCGHAZ (A3)	256	1350, 10	13, 23		256	700, 10	13, 23
SCRFGHAZ (A4)	100	900, 10	12, 25		100	900, 10	12, 25
ICRFGHAZ (A5)	100	900, 10	12, 25		100	700, 10	12, 25
IRHAZ (A6)	56	700, 10	8, —		56	700, 10	8, —
SRHAZ (A7)	45	650, 10	7, —		45	650, 10	7, —

*UCGHAZ: unaltered coarse-grained HAZ, SCRCGHAZ: supercritically reheated coarse-grained HAZ, ICRCGHAZ: intercritically reheated coarse-grained HAZ, SCRFGHAZ: supercritically reheated fine-grained HAZ, ICRFGHAZ: intercritically reheated fine-grained HAZ, IRHAZ: intercritically reheated HAZ, and SRHAZ: subcritically reheated HAZ.

**$\Delta t_{8/5}$: cooling time between 800 °C and 500 °C.

observed by an optical microscope, a scanning electron microscope (SEM), and a transmission electron microscope (TEM), and their phases were analyzed by Mossbauer spectroscopy.

Mossbauer spectroscopy is advantageous for its ability to provide qualitative and quantitative information on the fraction of iron-containing phases in steels, which is hard to obtain from other analysis methods such as X-ray analysis. The present study employs Mossbauer spectroscopy to identify the phases present in the simulated HAZ specimens and

Table V. Initial Hyperfine Parameters at 300 K

Phase	Spectrum	δ (mm/s)	Q (mm/s)	H_f (T)	Reference
Bcc	bcc-Fe	0.00	0.00	33.0	standard
Bcc + bct	Fe-M(1)	0.11	0.02	27.4	our work
	Fe-M(2)	0.07	−0.04	30.7	
Bct	bct-Fe(1)	0.08	0.28	26.5	14
	bct-Fe(2)	−0.05	0.20	34.3	
	bct-Fe	0.06	−0.18	33.3	
Fcc	fcc-Fe	−0.05	0.00	0.00	15
Fe_3C	Fe_3C(a)	0.21	−0.06	19.7	our work 16 to 18
	Fe_3C(b)	0.19	0.32	20.5	
	Fe_3C(s)	0.41	1.74	0.0	
Fe_5C_2	Fe_5C_2	0.10	0.12	23.0	our work

to quantitatively measure their fractions. A ^{57}Co gamma ray source with 50 milli-Curie and disc specimens of 10 mm in diameter and about 50 μm in thickness were used for Mossbauer spectroscopy. With each pure phase prepared, initial hyperfine parameters for the samples were determined.

Table V shows initial hyperfine parameters of each phase,[14–18] *e.g.*, austenite (fcc-Fe), martensite (bct-Fe), ferrite (bcc-Fe), and carbides (Fe_3C). The phase fractions were determined with the least-squares fitting, which was performed on the measured Mossbauer spectra. Each phase constitutes a couple of subspectra depending on the environment of iron atoms, and they are denoted by the number (or character) inside the parentheses (Table V). Problems in the interpretation of Mossbauer spectra were resolved as follows. First, Mossbauer spectroscopy alone cannot differentiate the ferrite in pure ferrite from the ferrite in bainite or pearlite. They were analyzed as bcc-Fe (ferrite) as a total. Second, the classification of Mossbauer subspectra of ferrite and martensite becomes difficult when iron atoms have neighboring alloy elements. They were collectively analyzed as Fe-M(M: alloying element), which was then allocated into each phase according to the fractional ratio of bcc-Fe and bct-Fe.

III. RESULTS

A. *Mossbauer Spectroscopy*

Table V lists the reported hyperfine parameters with which the least-squares fitting of the Mossbauer spectra can be conducted. Pure ferrite has a single sextet (bcc-Fe), whose hyperfine field is about 33 Tesla. The bct phase (martensite), however, includes a significant amount of carbon at the interstitial sites. Thus, the spectrum consists of at least 3 sextets, *i.e.*, bct-Fe(1), bct-Fe(2), and bct-Fe, depending on the location of carbon atoms at the first and second nearest interstitial sites, and further. Substitutional elements, such as manganese and silicon, are soluble in both bcc and bct structures, and strongly disturb the local environment of iron atoms to produce several subspectra. Due to the strong disturbance, there seems to be no resolution to differentiate the patterns of bct-Fe and bcc-Fe, where substitutional elements are incorporated. The only choice is to designate the spectra simply as Fe-M(1) and Fe-M(2) for those Fe's with an alloying element at the first and the second nearest substitutional sites, respectively. (When the element locates farther apart, the spectrum becomes bcc-Fe or bct-Fe.) The nonmagnetic fcc phase (austenite) has a highly isotropic structure and produces a singlet. Fe_3C carbide has two equivalent sites in the crystal structure and thus produces two magnetic sextets. The hyperfine magnetic fields are 20.5 and 19.7 T for Fe_3C(a) and Fe_3C (b), respectively. In a rapidly cooled sample, some cementites should be very fine. This requires an extra spectrum for superparamagnetic cementite, Fe_3C(s), to analyze the sample where martensite and/or bainite are the constituents.

The integral intensity of each subspectrum (the area below the base line) provides an estimation of iron population in each phase. The volume fractions of steel phases have hardly been mentioned in the Mossbauer spectrum analysis, since the gamma ray recoil-free fractions are not exactly known for the phases. At a constant experimental temperature, however, the recoil-free fraction is solely determined by the Debye temperature of the phase. The Debye temperatures are about 470 K for bcc-Fe and 480 K for Fe_3C. The value for the bct-Fe is not available at this moment, but should be in between 470 K (bcc-Fe) and 480 K (Fe_3C) as the mechanical rigidity of the bct-Fe is. Such a negligible difference in the Debye temperatures implies that the area fraction of a subspectrum well represents the atomic population of iron in each phase without a serious correction for the recoil-free fraction. Furthermore, the atomic fraction and the volume fraction differ less than 10 pct (relative), since the volume per iron atom is about 12 A^3 in iron phases (bcc, bct, and fcc) and is about 13 A^3 in carbides. (The volume per iron atom was obtained by dividing the volume of a unit cell with the number of iron atoms in the cell.) In these regards, the area fraction of the subspectrum is a good estimation of the fraction of the corresponding phase. It should be noted that the bcc phase could be the constituent of pure ferrite, pearlitic ferrite, and bainitic ferrite. Thus, the relevant structure must be assigned with the help of the microstructural observations.

Figures 3(a) through (f) show Mossbauer spectra of the base metal and the simulated HAZ specimens. It was found that the fitted hyperfine parameters were very close to the initial parameters of Table V, regardless of the HAZ specimen. Thus, the peak positions of subspectra are marked only at the top of the figure. The fraction of each phase was obtained by integrating the resonance absorption area of subspectrum, and the results are provided in Table VI. Figure 3(a) is the Mossbauer spectrum of the base metal, composed of 97 pct (vol pct) ferrite (or bainite) and 3 pct carbide. The

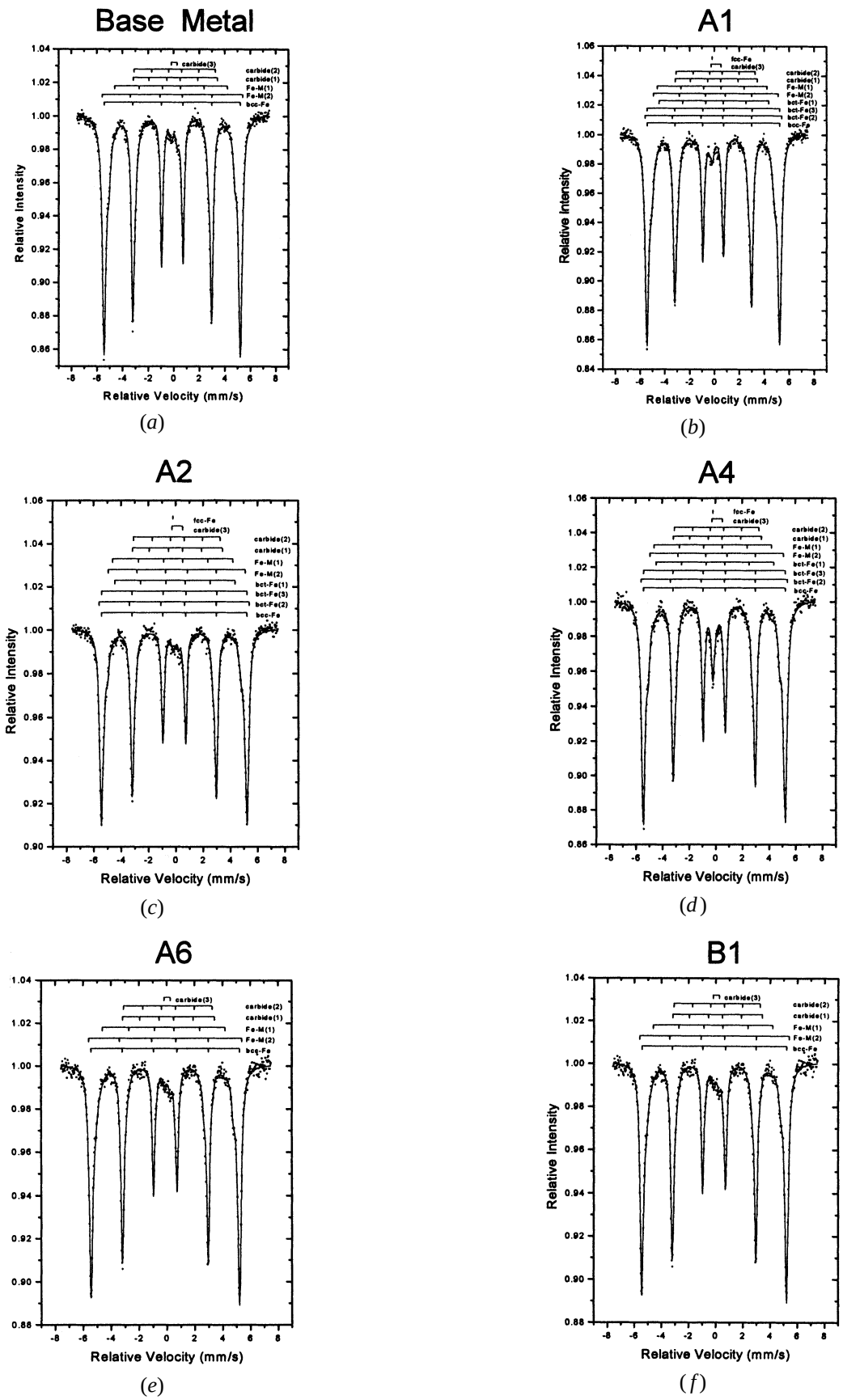

Fig. 3—Mossbauer spectra of (*a*) the base metal and (*b*) through (*f*) the simulated HAZ specimens: (b) A1, (c) A2, (d) A4, (e) A6, and (f) B1 specimens.

Table VI. Volume Fraction of Phases Analyzed from Mössbauer Spectroscopy (Error Range, ±1 Percent)

Specimen	T_p^1 (°C)	T_p^2 (°C)	Volume Fraction of Phases (Pct)			
			Ferrite	Martensite	Austenite	Carbide*
Base metal	—	—	97	0	0	3
A1	1350	1350	4	93	2	1
A2	1350	900	58	39	1	2
A3	1350	700	11	87	0	2
A4	900	900	71	22	5	2
A5	900	700	77	18	3	2
A6	700	700	96	0	0	4
A7	650	650	97	0	0	3
B1	1350	1350	95	0	0	5
B2	1350	900	96	0	0	4
B3	1350	700	96	0	0	4
B4	900	900	96	0	0	4
B5	900	700	97	0	0	3
B6	700	700	94	0	0	6
B7	650	650	94	0	0	6

* All carbides including Fe_3C cementites.

A1 specimen consists of 93 pct martensite, 4 pct ferrite, 1 pct carbide, and 2 pct retained austenite (Figure 3(b)). In the A2 specimen with $T_p^2 = 900$ °C, the martensite fraction is considerably reduced to 39 pct, whereas the ferrite fraction increases to 58 pct (Figure 3(c)). The A3 specimen with $T_p^2 = 700$ °C is mostly composed of martensite (87 pct) because it is slightly affected by tempering at T_p^2 after martensite is formed by T_p^1. The A4 and A5 specimens with $T_p^1 = 900$ °C are mainly composed of ferrite, together with minor presence of 20 pct martensite, 3 to 5 pct austenite, and 2 pct carbide (Figure 3(d)). The A6 and A7 specimens with T_p below the A_1 temperature are mainly composed of ferrite, together with no observation of martensite subspectrum (Figure 3(e)). Figure 3(f) is a spectrum of the B1 specimen, being the A1 specimen after PWHT, which is composed of more than 95 pct ferrite with complete extinction of martensite. Other PWHT specimens show almost the same spectrum as the B1 specimen, indicating the nonexistence of martensite after PWHT.

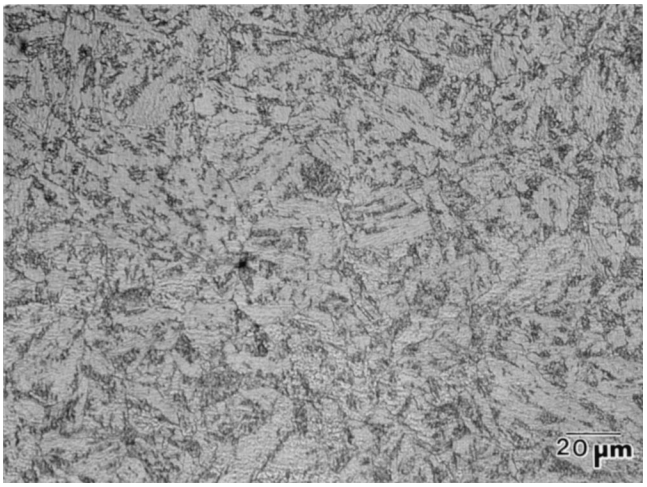

Fig. 4—Optical micrograph of the base metal of the SA 508 steel.

B. *Microstructure*

Figure 4 is an optical micrograph of the base metal, showing that it consists of upper bainite. Figures 5(a) through (g) are optical micrographs of the simulated HAZ specimens. The A1 through A3 specimens have large prior austenite grains and contain lots of martensite (Figures 5(a) through (c)). The A4 and A5 specimens do not seem to contain much martensite, rather showing similar microstructures to that of the base metal, together with a tendency of refinement (Figures 5(d) and (e)). The prior austenite grain size was measured to be 410 and 10 μm for the A1 specimen ($T_p = 1350$ °C) and the A4 specimen ($T_p = 900$ °C), respectively. The decrease in martensite might be because the decrease in the prior austenite grain size leads to acceleration of grain boundary nucleated bainite reaction, and because the reduction in cooling rate allows austenite to intersect the nose of a continuous cooling curve for bainite. Microstructures of the A6 and A7 specimens are almost the same as those of the base metal, but tend to be slightly decomposed (Figures 5(f) and (g)). The base metal does not change much after PWHT because it was tempered at 660 °C for 10 hours prior to PWHT, although the carbide size is somewhat increased. The HAZ microstructures of the B1 through B7 specimens after PWHT are similar to those before PWHT, but the overall structures become unclear and show a tendency of decomposition (Figures 6(a) through (g)).

For detailed microstructural analyses, A1, A2, A4, and A6 specimens were observed by SEM and TEM. Figure 7(a) is an SEM micrograph of the A1 specimen, showing martensite containing fine carbides. However, in the A2 specimen, a considerable amount of bainite (or ferrite) exists besides martensite (Figure 7(b)), consistent with the quantitative Mossbauer analysis data of Table VI. An SEM micrograph of the A4 specimen shows the presence of isolated, irregular-shaped structures, as marked by arrows, as well as fine bainite (Figure 7(c)). A TEM micrograph of the irregular-shaped structures is shown in Figure 8(a). These structures, known as martensite islands, are mostly composed of

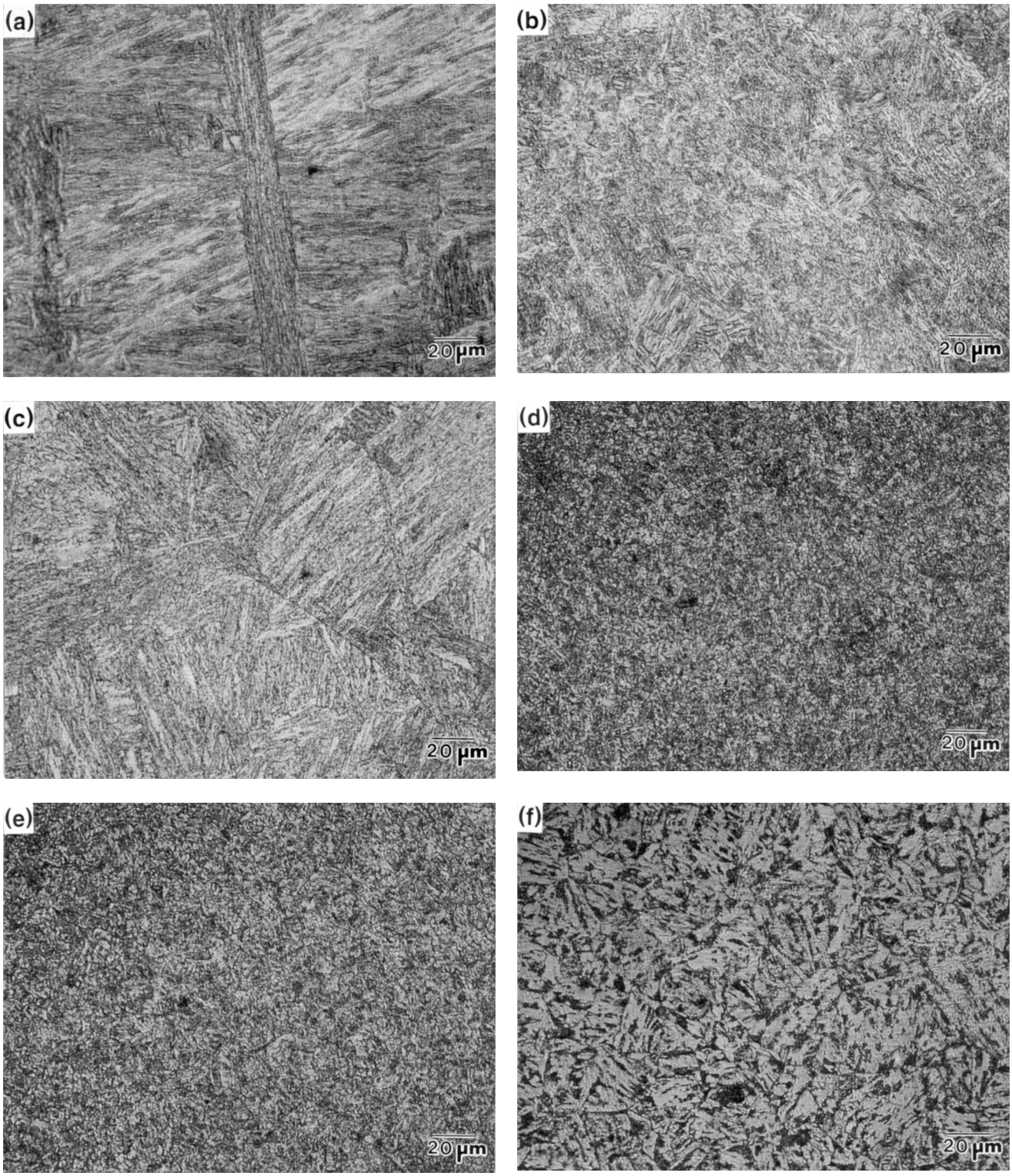

Fig. 5—Optical micrographs of (*a*) A1, (*b*) A2 (*c*) A3, (*d*) A4, (*e*) A5, (*f*) A6. Continued.

lath martensite, but are also called martensite-austenite (M-A) constituents because a small amount of retained austenite is found along martensite lath boundaries.[2,10] Twinning is also observed, as shown in Figure 8(b). The volume fraction of martensite islands in the A4 specimen is about 20 pct, well correlating with the Mossbauer analysis data of Table VI. It is interesting to note that as their fraction increases, the fraction of austenite also increases and reaches 3 to 5 pct. An SEM microstructure of the A6 specimen is almost similar to that of the base metal (Figure 7(d)).

Figures 9(a) and (b) are SEM micrographs of the B1 and B6 specimens. Although the overall microstructures are

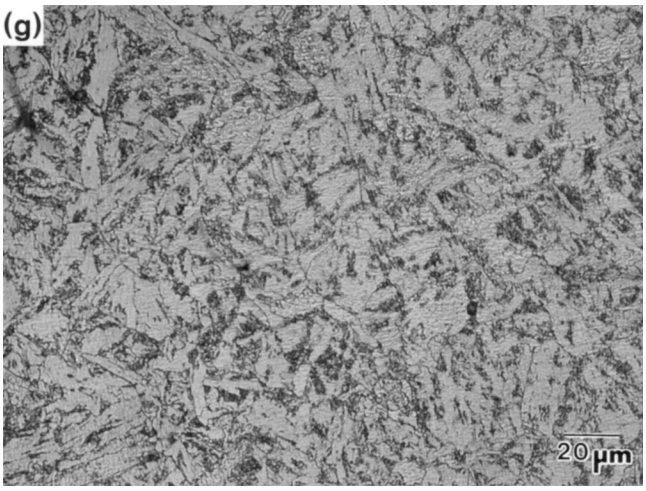

Fig. 5—Continued. (*g*) A7 specimens.

similar to those before PWHT, it is observed that the carbide volume fraction considerably increases, which matches well with the Mossbauer data.

C. *Mechanical Properties*

Table VII provides hardness, tensile strength, and Charpy impact absorbed energy of the simulated HAZ specimens. Hardness improves by two to three times over the base metal with increasing T_p owing to the martensitic formation. With lowering T_p, the ferrite-bainite fraction increases, whereas the martensite fraction decreases because the cooling rate slows down; thus, hardness does not show much improvement over the base metal. When T_p is below the A_1 temperature where only tempering occurs, hardness is rather lower than that of the base metal. The same trend applies to tensile strength. Tensile strengths of the A1 through A5 specimens increase as the martensite fraction increases (Table VI), while the A6 and A7 specimens under tempering effect alone have lower tensile strengths than that of the base metal. The B1 through B7 specimens show considerably lower tensile strengths than those of the A1 through A7 specimens, but the trend is the same.

Absorbed impact energy shows an opposite trend to tensile strength and hardness (Table VII). The A1 through A7 specimens show lower impact energy than that of the base metal. Especially, the coarse-grained HAZs of the A1 through A3 specimens have extremely low impact energy. The impact energy of the A6 and A7 specimens is almost the same as the base metal, whereas the A4 and A5 specimens show intermediate values between the A6 and A1 specimens. After PWHT, the HAZ specimens show an opposite trend to pre-PWHT. The A6 and A7 specimens having high impact energy before PWHT show the lowest impact toughness after PWHT, while the B1 through B5 specimens show greatly improved impact energy after PWHT in comparison to the A1 through A5 specimens. The impact energy of the B6 and B7 specimens further deteriorates below the base metal and the coarse-grained HAZ specimens, indicating that the subcritical HAZ becomes the most brittle region after PWHT.

Figures 10(a) and (b) are SEM fractographs of the A1 and A4 specimens, showing cleavage fracture in the A1 specimen having low impact energy but ductile fracture in the A4 specimen having high impact energy.

IV. DISCUSSION

A. *Microstructural Analysis of Thermally Simulated HAZ*

In this study, phases of the thermally simulated HAZ of the 508 steel, which has very complex microstructures, were analyzed by Mossbauer spectroscopy, and then compared with microstructural observations to examine the applicability and reliability of Mossbauer spectroscopy.

The base metal is mainly composed of upper bainite (Figure 4), but the microstructures of its HAZ are tremendously changed with welding thermal cycles. Since the A1 specimen with both T_p^1 and T_p^2 being 1350 °C was cooled after reheating to the upper austenite region, it is mainly composed of martensite (Figure 5(a) and Table VI). The A3 specimen, where T_p^1 is 1350 °C and T_p^2 is 700 °C, also shows mostly martensite, as in the A1 specimen, because it is only slightly affected by T_p^2 after martensite is already formed by T_p^1 (Figure 5(c)). However, in the A2 specimen where T_p^1 is 1350 °C and T_p^2 is 900 °C, martensite formed by T_p^1 cools down after reheating up to the lower austenite region, and thus the martensite fraction is lower than that of the A1 specimen. This is associated with the formation of bainite as well as martensite because the slope of the cooling curve at T_p = 900 °C is smaller than the case of T_p = 1350 °C, as shown in Figure 1. Figure 7(b) confirms the coexistence of martensite and bainite. In the A4 specimen where both T_p^1 and T_p^2 are 900 °C, the two thermal cycles rise up to the lower austenite region and then gradually cool down; thus, the martensitic formation is further reduced to 20 pct (Figure 7(c) and Table VI). Since the martensite fraction is relatively small here and mainly formed between bainite laths and prior austenite grain boundaries, it has an isolated island shape,[2,10] and typically contains a considerable amount of austenite (Table VI). The microstructure of the A5 specimen with T_p^2 = 700 °C is not changed much from that of the A4 specimen because of the only minor tempering effect (Figure 5(e)). The A6 and A7 specimens subjected to double thermal cycles of 700 °C or 650 °C show similar microstructures to that of the base metal (Figures 5(f) and (g)). Although their carbide fractions are somewhat higher than that of the base metal, according to the Mossbauer spectroscopic data of Table VI, it is hard to be confirmed since the variations are within the error range.

The overall microstructures of the B1 through B7 specimens subjected to PWHT are similar to each other compared with the A1 through A7 specimens (Figures 6(a) through (g)). However, martensite is transformed to tempered martensite, and the total carbide fraction increases because of the additional carbide precipitation (Table VI). Figures 11(a) and (b) are TEM micrographs of the carbon-extraction replicas obtained from the base metal and the B6 specimen, respectively. It is noted that carbides of the B6 specimen are coarser than those of the base metal, and that their fraction is higher because of the repeated thermal effect on the B6 specimen. Consequently, the Mossbauer spectroscopic data indicate that their microstructures are composed of only ferrite and carbides.

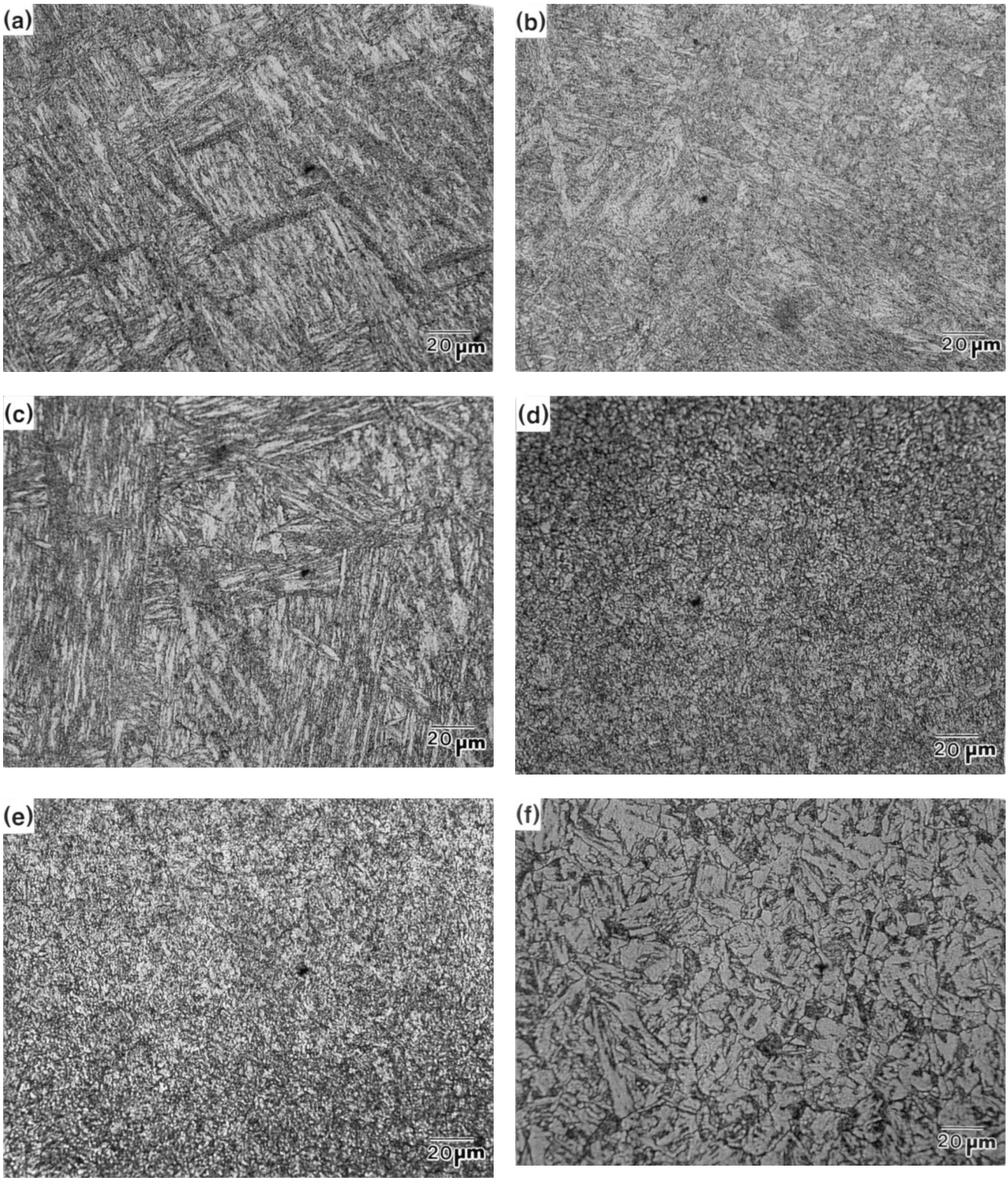

Fig. 6—Optical micrographs of (*a*) B1, (*b*) B2, (*c*) B3, (*d*) B4, (*e*) B5, (*f*) B6. Continued.

The results of Mossbauer spectroscopy correlate well with the microstructural observations. Thus, it is found from this study that Mossbauer spectroscopy proves very useful for understanding the complex HAZ microstructures of the SA 508 steel weld because it provides essential information on phase transformation in the HAZ.

B. *Correlation of Microstructure and Fracture Toughness*

As shown from the microstructural observations and the Mossbauer spectroscopic data, the HAZ undergoes phase transformation according to thermal cycles. When T_p rises

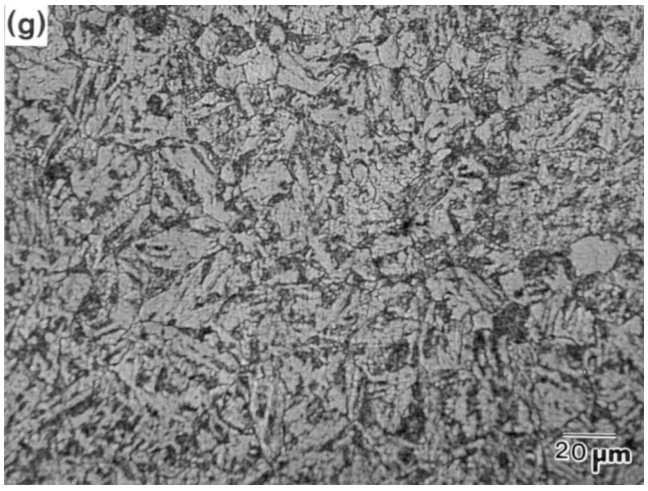

Fig. 6—Continued. (*g*) B7 specimens. These specimens were subjected to PWHT.

up to the austenite region and then rapidly cools down, martensite is mostly formed, and thus enhances hardness and strength of the HAZ over the base metal. On the other hand, the only tempering effect is added when T_p rises to below the A_1 temperature, and slightly reduces hardness and strength, compared with the base metal (Table VII). However, impact toughness shows an opposite trend to hardness and strength, and decreases with increasing the martensite fraction. This is confirmed by the impact-toughness data of the A1 through A7 specimens, as shown in Table VII. In contrast, impact toughness of the B1 through B7 specimens subjected to PWHT, where all martensite formed before PWHT is transformed to tempered martensite, shows a different trend than the A1 through A7 specimens. Particularly, the A6 and A7 specimens having high impact toughness before PWHT show the lowest toughness after PWHT in the B6 and B7 specimens. These specimens are of the subcritical HAZ region where T_p has only risen to below the A_1 temperature, turning into the LBZ having the lowest impact toughness after PWHT. This contradicts the impact toughness results of the typical steel HAZ.

To investigate the microstructural factors affecting the impact toughness reduction of the B6 and B7 specimens, the deformed area beneath the fractured surface of the tensile specimen of the B6 specimen was observed by an SEM (Figure 12). Many carbides were found along lath boundaries or inside laths of upper bainite, with the former being coarser

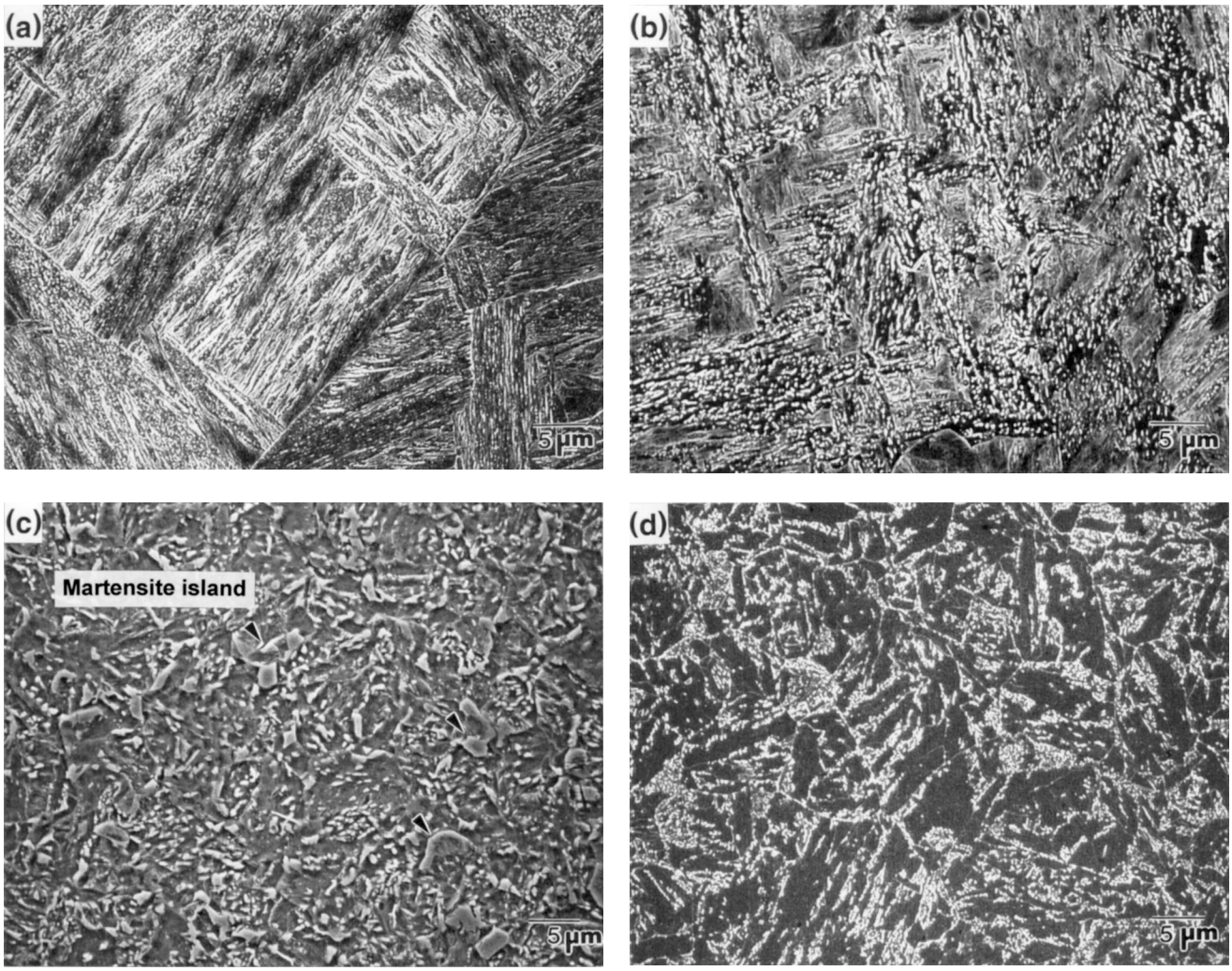

Fig. 7—SEM micrographs of (*a*) A1, (*b*) A2, (*c*) A4, and (*d*) A6 specimens.

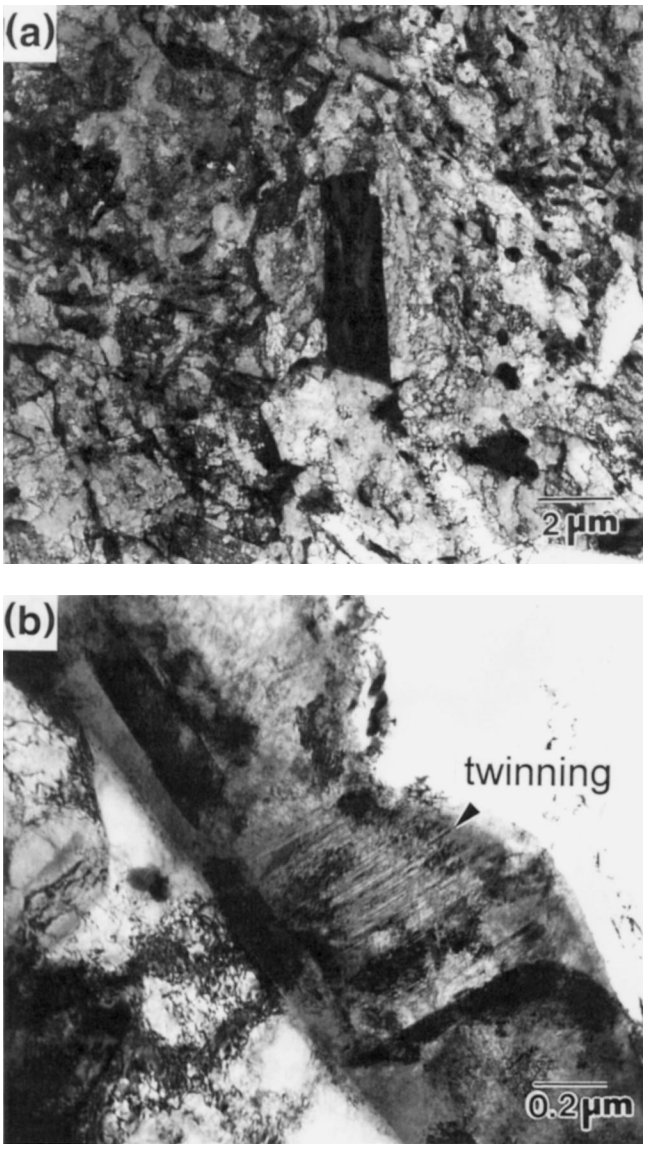

Fig. 8—TEM micrographs of A4 specimen, showing (*a*) irregular-shaped martensite islands and (*b*) twinning.

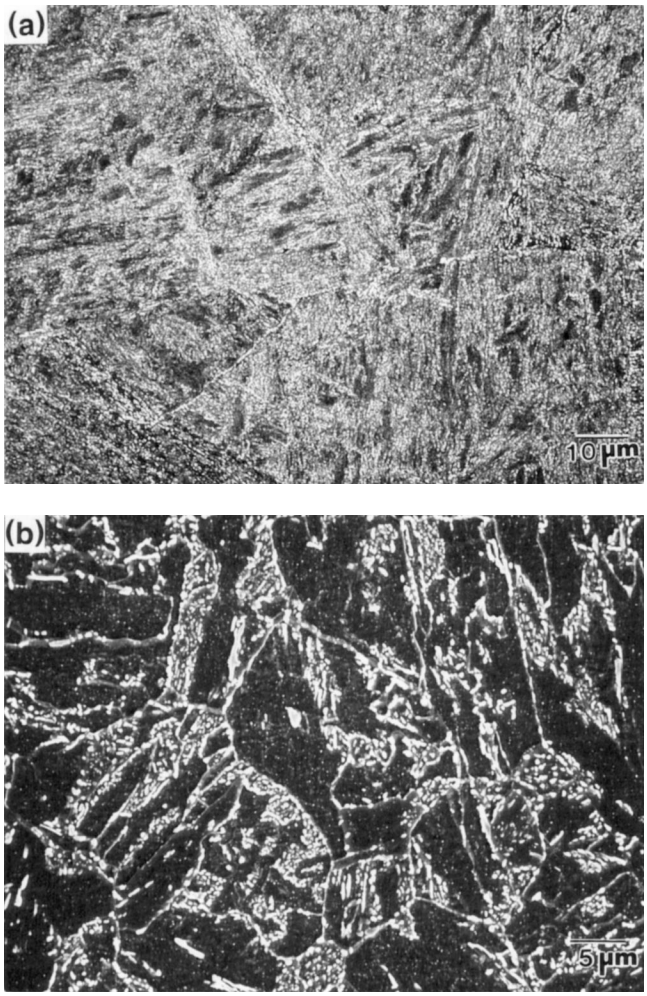

Fig. 9—SEM micrographs of (*a*) B1 and (*b*) B6 specimens. These specimens were subjected to PWHT.

Table VII. Hardness, Tensile Strength, and Charpy Impact Absorbed Energy of Thermally Simulated HAZ Specimens

Specimen	T_p^1 (°C)	T_p^2 (°C)	Vickers Hardness (VHN)	Tensile Strength (MPa)	Charpy Absorbed Energy at −50 °C (J)
Base metal	—	—	198	610	97
A1	1350	1350	460	1286	12
A2	1350	900	374	1327	10
A3	1350	700	333	1206	14
A4	900	900	316	1039	46
A5	900	700	282	826	49
A6	700	700	194	558	90
A7	650	650	196	586	85
B1	1350	1350	288	767	85
B2	1350	900	258	780	150
B3	1350	700	294	749	120
B4	900	900	227	670	175
B5	900	700	216	637	160
B6	700	700	186	537	22
B7	650	650	189	559	20

than the latter. Voids were mostly observed at the interfaces between carbides and the matrix when coarse interlath carbides were aligned parallel to the tensile direction, whereas no voids were formed at fine carbides within laths. It is found from these observations that coarse interlath carbides are main sites of void initiation and growth. Thus, fracture toughness is lowered with increasing the carbide fraction. According to the Mossbauer spectroscopic data of Table VI, the B1 through B7 specimens are all composed of ferrite (or bainite) and carbides, and the B6 and B7 specimens show the largest carbide fraction and thus the lowest impact toughness. The lower carbide fractions in the B1 through B5 specimens than in the B6 and B7 specimens are because most carbides present in the base metal are dissolved by thermal cycles of reheating to the austenite region and cooling, and then reprecipitated during PWHT. Thus, the B1 through B5 specimens composed of tempered martensite show higher impact toughness than the B6 and B7 specimens having tempered bainite and the large carbide fraction.

The toughness results of the 508 steel HAZ indicate that the microstructural factors affecting the toughness data critically depend on the application of PWHT. In other words,

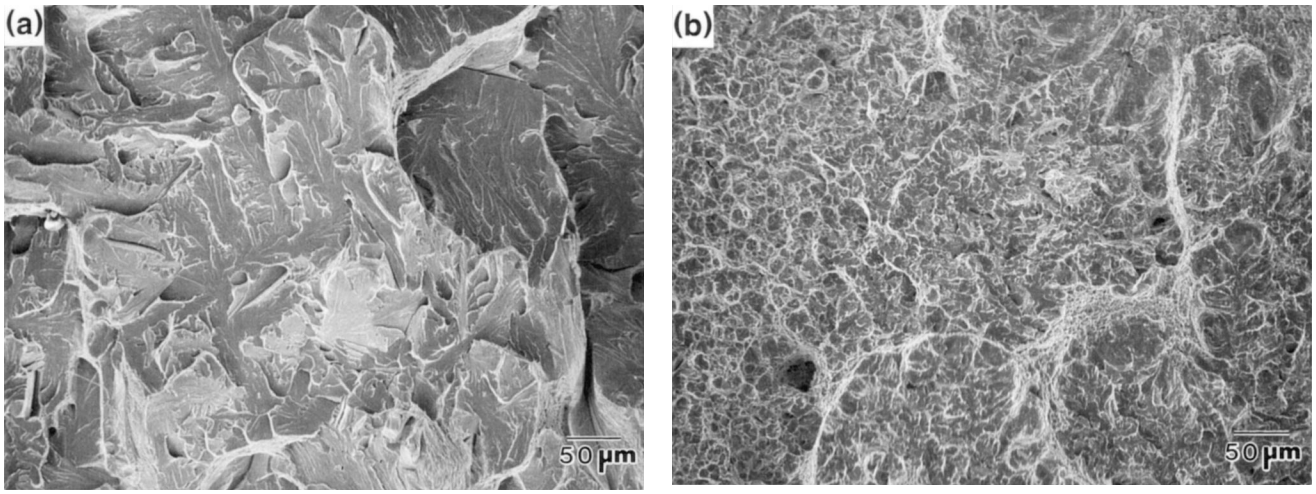

Fig. 10—SEM fractographs of (*a*) A1 and (*b*) A4 specimens.

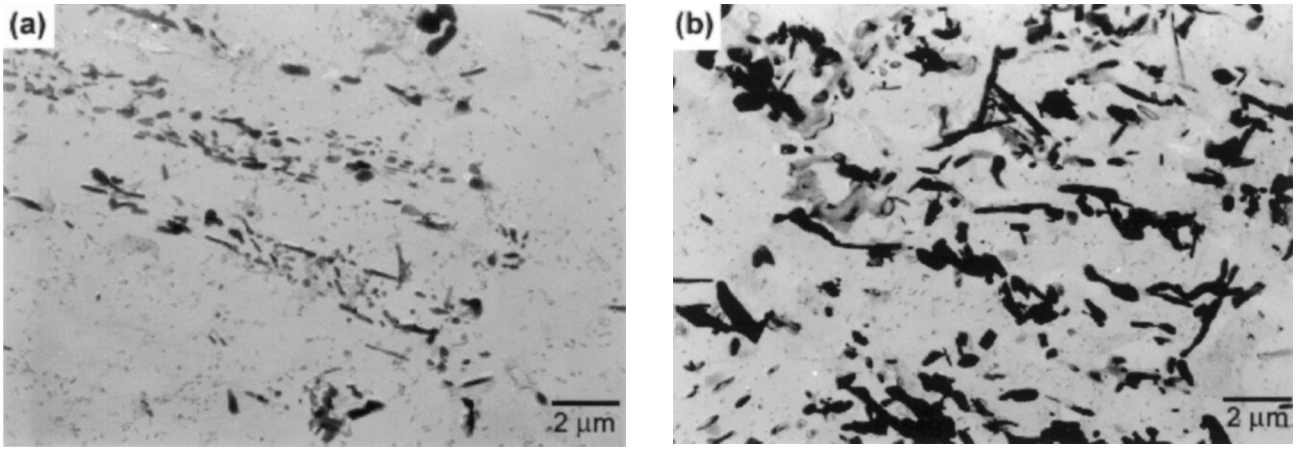

Fig. 11—TEM micrographs of the carbon extraction replicas obtained from (*a*) the base metal and (*b*) B6-specimen.

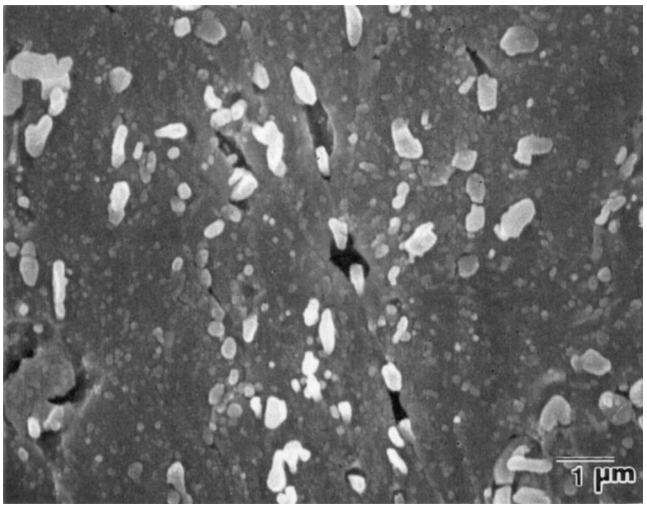

Fig. 12—SEM micrograph of B6 specimen sectioned parallel to the tensile axis, showing the deformed area beneath the fracture surface of the tensile specimen.

the martensite fraction significantly affects impact toughness in the HAZ before PWHT, whereas the carbide fraction does so in the HAZ after PWHT. Under the PWHT condition applied to components for atomic power plants, the subcritical HAZ region showing the largest carbide formation becomes the LBZ, which greatly contradicts conventional understanding that the LBZ is the coarse-grained HAZ. In addition, PWHT, which is applied practically in order to improve fracture toughness of the 508 steel HAZ, increases the size and volume fraction of carbides. These carbides act as fracture initiation sites, and thus considerably deteriorate fracture toughness. Therefore, PWHT, which has been applied without questioning, should be reconsidered according to the alloy composition and the welding condition, and the PWHT condition should be well established in close relation with the HAZ microstructures. Also, further studies should be made on alloy design, heat treatment, and welding and PWHT conditions to better control the formation of carbides.

V. CONCLUSIONS

In this study, microstructural factors affecting fracture toughness of the SA 508 steel HAZ were investigated with the following conclusions.

1. Phases present in the thermally simulated HAZ were

identified, and their volume fractions were quantitatively measured using Mossbauer spectroscopy. Specimens with the peak temperature raised to 1350 °C show mostly martensite, but the microstructures are not changed much from the base metal due to the minor tempering effect alone when it is raised to 650 °C or 700 °C. With the peak temperature raised to 900 °C, the martensite fraction is reduced, while bainite or martensite islands are formed because of the slow cooling from the lower austenite region. The overall microstructures of the simulated HAZ after PWHT are similar to those before PWHT, but all martensite formed before PWHT is tempered after PWHT, together with the increase in the carbide volume fraction because of the additional carbide precipitation.

2. As the volume fraction of martensite present inside the HAZ increases, hardness and strength increase, but fracture toughness decreases. However, fracture toughness after PWHT depends on the carbide volume fraction, and increases with increasing the carbide fraction since all martensite is transformed to the tempered martensite after PWHT. The subcritical HAZ, where a large amount of carbides are formed, becomes a local brittle zone. Consequently, the microstructural factor affecting fracture toughness of the HAZ are the martensite fraction before PWHT, and the carbide fraction after PWHT. Thus, PWHT plays a important role in evaluating fracture toughness of the HAZ.
3. The Mossbauer spectroscopic results are well correlated with the microstructural observations, and thus enable one to identify the phases which are hard to identify microstructurally and to analyze them quantitatively. Therefore, Mossbauer spectroscopy can be useful in the microstructural analysis of the HAZ.

ACKNOWLEDGMENTS

This work was supported by the Korea Atomic Energy Research Institute. The authors thank Dr. Yong Jun Oh, Korea Atomic Energy Research Institute, and Mr. Ki Ok Nam, Pohang Iron and Steel Co., Ltd., for their helpful discussion on the thermal simulation analysis. One of the authors (SJO) appreciates the postdoctoral fellowship from the Korean Science and Engineering Foundation.

REFERENCES

1. H.G. Pisarski and J. Kudoh: in *Welding Metallurgy of Structural Steels*, J.Y. Koo, ed., TMS, Denver, CO, 1987, pp. 263-75.
2. B.C. Kim, S. Lee, N.J. Kim, and D.Y. Lee: *Metall. Trans. A*, 1991, vol. 22A, pp. 139-49.
3. K. Uchino and Y. Ohno: *Proc. 7th Int. Conf. on Offshore Mechanics and Arctic Engineering*, Houston, TX, ASME, Golden, CO, 1988, pp. 159-65.
4. S. Lee, B.C. Kim, and D. Kwon: *Metall. Trans. A*, 1993, vol. 24A, pp. 1133-41.
5. D.P. Fairchild: in *Welding Metallurgy of Structural Steels*, J.Y. Koo, ed., TMS, Denver, CO, 1987, pp. 303-18.
6. S. Lee: *Scripta Metall.*, 1988, vol. 22, pp. 59-64.
7. K. Easterling: *Introduction to the Physical Metallurgy of Welding*, Butterworth and Co., London, 1983, ch. 1.
8. G.R. Wang, T.W. Lau, G.C. Weatherly, and T.H. North: *Metall. Trans. A*, 1989, vol. 20A, pp. 2093-2100.
9. J.Y. Koo and A. Ozekcin: in *Welding Metallurgy of Structural Steels*, J.Y. Koo, ed., TMS, Denver, CO, 1987, pp. 119-35.
10. S. Lee, B.C. Kim, and D. Kwon: *Metall. Trans. A*, 1992, vol. 23A, pp. 2803-16.
11. T.D. Park, K.K. Baek, and D.S. Kim: *Metall. Mater.*, 1997, vol. 3, pp. 46-50.
12. P.G. Debrunner and H. Frauenfelder: in *An Introduction to Mossbauer Spectroscopy*, L. May, ed., Plenum Press, New York, NY, 1971, pp. 155-76.
13. G.J. Long: in *Mossbauer Spectroscopy Applied to Inorganic Chemistry*, G.J. Long, ed., Plenum Press, New York, NY, 1984, pp. 7-25.
14. J.R. Genin: *Metall. Trans. A*, 1987, vol. 18A, pp. 1371-88.
15. H. Ino, T. Moriya, F.E. Fujita, Y, Maeda, Y. Ono, and Y. Inokuti: *J. Phys. Soc. Jpn.*, 1968, vol. 25, pp. 88-99.
16. M. Ron and Z. Mathalone: *Phys. Rev. B*, 1971, vol. 4, pp. 774-77.
17. F. Aubertin, L. Abada, and U. Gonser: *Hyp. Int.*, 1998, vol. 111, pp. 201-04.
18. M. Ron, H. Shechter, and S. Niedzwidz: *J. Appl. Phys.*, 1968, vol. 39, pp. 265-75.
19. B. Fultz: in *Mossbauer Spectroscopy Applied to Magnetism and Materials Science*, G.J. Long and F. Grandjean, eds., Plenum Press, New York, NY, 1993, pp. 1-26.
20. D. Rosenthal: *Trans. ASME*, 1946, Nov., pp. 849-66.
21. J.H. Kim and E.P. Yoon: *J. Kor. Inst. Met. Mater.*, 1998, vol. 36, pp. 1329-37.
22. K. Suzuki: in *Neutron Irradiation Effects in Solids*, M.A. Kirk, ed., NHC, Argonne, IL, 1981, pp. 443-50.